

# Ultra-thin Unidirectional Holographic Metasurface Antenna Excited by TE-Mode Surface Wave

Byeongjin Kim, *Graduate Student Member, IEEE*, Seungwoo Bang, *Graduate Student Member, IEEE*, Sumin Yun, Maengchang Kang, *Graduate Student Member, IEEE*, Hosaeng Kim, *Member, IEEE*, and Jungsuek Oh, *Senior Member, IEEE*

**Abstract**—This letter proposes an ultra-thin unidirectional holographic metasurface (HM) antenna (HMA) based on TE-mode surface waves excited over an artificial magnetic conductor (AMC) ground. It is found that replacing the conventional perfect electric conductor (PEC) ground with an AMC ground increases surface wave power ratio for ultra-thin HMAs, thereby achieving higher aperture efficiency. Key design considerations are examined in detail. A prototype is fabricated and measured in the 6G upper-mid band, achieving an ultra-low profile of  $0.025\lambda_0$  and a peak aperture efficiency of 29.5%.

**Index Terms**—holographic metasurface (HM), artificial magnetic conductor (AMC), low profile, 6G upper-mid band.

## I. INTRODUCTION

WHEN compact resonant antennas are integrated into large-form-factor platforms such as smartphones or vehicles, their performance often degrades due to nearby components that add loss and coupling [1]–[8]. In particular, surface waves on the electrically large outermost substrate can distort radiation patterns [8]. Holographic metasurface antennas (HMAs) [9]–[12] address this by shaping surface-wave energy into a prescribed radiating aperture, improving beam stability and enabling high-gain radiation [10].

Unlike commonly used metasurface antennas such as transmitarrays or reflectarrays for high-frequency applications [13]–[15], an HMA features a lower profile by sharing a single plane for the feed antenna and the metasurface. It employs a surface-wave launcher (SWL) as the feed to generate a surface wave on a grounded dielectric substrate (GDS) [9]–[12]. The surface-impedance-modulated HM unit cells (HMUCs) then convert this energy into a radiated wave in air.

Conventional unidirectionally radiating HMAs often utilize a perfect electric conductor (PEC) ground and TM-mode surface waves [16]–[30]. Several studies have focused on maximizing the aperture efficiency of PEC-grounded HMAs [25]–[30]. However, as the dielectric thickness becomes thinner than a quarter wavelength and approaches zero, the ratio

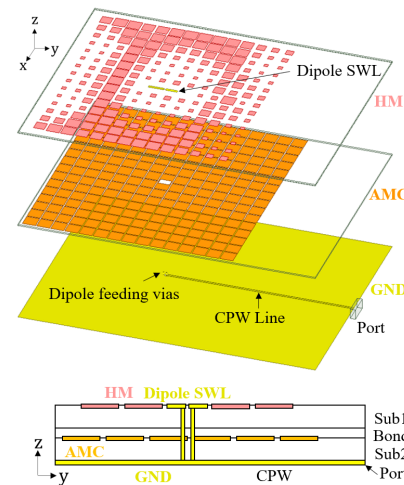


Fig. 1. Configuration of the proposed HMA featuring a low profile and high efficiency. The marked design parameters are  $(S_x, S_y, l_{margin}, l_{dipole}, C_y, C_x, g_{via}, h_{sub}, h_{bond}) = (45, 43, 15, 5.6, 2.2, 1.4, 0.6, 0.254, 0.038)$  mm.

of evanescent decaying power to the power guided along the surface increases exponentially [18], [31]. This phenomenon makes it challenging to maintain high aperture efficiency with a PEC ground when designing an ultra-low-profile HMA.

Another category of HMAs that achieve unidirectional radiation employs TE-mode surface waves together with a reflector. In this approach, TE-mode HMAs operate without a directly integrated ground and therefore radiate to both sides of the dielectric substrate with low aperture efficiency [32]–[38]. To enforce unidirectional radiation and improve aperture efficiency, an artificial magnetic conductor (AMC) ground is used as a reflector to reduce total thickness [37], [38]. In these studies, however, proximate integration of the TE-mode HM with the AMC ground was not feasible because it inevitably distorted the pre-designed HM. Consequently, the resulting profiles exceed 0.17 wavelength.

This letter proposes an ultra-thin unidirectional AMC-ground-integrated HMA excited by a TE-mode surface wave, featuring an ultra-thin 0.025 wavelength profile (Fig. 1). Compared with [37] and [38], our contributions are twofold: (1) a theoretical and experimental analysis demonstrating that an AMC ground enables an ultra-thin profile with high aperture efficiency; and (2) a design procedure for proximate integration of the SWL and HMUCs with the AMC ground.

Manuscript created October, 2025;

This work was supported in part by Samsung Electronics Co., Ltd., and in part by an Institute of Information and Communications Technology Planning and Evaluation (IITP) through the Korean Government [Ministry of Science and ICT (MSIT)], “Innovative Fusion Technologies of Intelligent Antenna Material/Structure/Network for THz 6G,” under Grant 2021-0-00763. (Corresponding author: Jungsuek Oh.)

Byeongjin Kim, Seungwoo Bang, Maengchang Kang, and Jungsuek Oh are affiliated with the Institute of New Media and Communications (INMC), Department of Electrical and Computer Engineering, Seoul National University, Seoul 08826, South Korea (e-mail: jungsuek@snu.ac.kr).

Sumin Yun and Hosaeng Kim are with Samsung Electronics Co., Ltd., Suwon, South Korea.

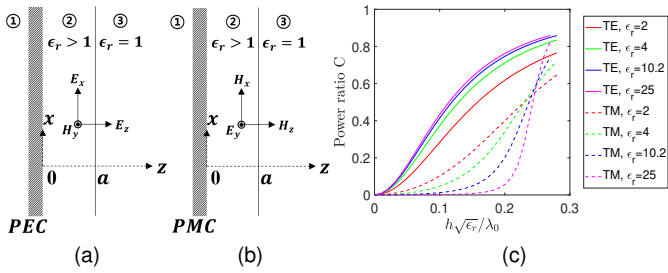


Fig. 2. Geometry for a surface wave propagating in the  $x$ -axis direction, with (a) PEC ground and (b) PMC ground. (c) The power ratio of the guided surface wave power over the total power including evanescent decaying power for TE and TM modes with  $\epsilon_r = 2, 4, 10.2, 25$ .

## II. SURFACE WAVE PROPAGATION IN PERFECT-MAGNETIC-CONDUCTOR GROUNDED DIELECTRIC SLAB

To design an HMA with a low profile and high aperture efficiency simultaneously, a high portion of the surface wave power should remain within the grounded dielectric slab while propagating tangentially along the surface, even if the slab thickness is small. Fig. 2 shows the scenario where the surface wave propagates along a uniform PEC or PMC grounded dielectric interface. With the conventional PEC ground, the TM mode power ratio,  $C_{TM}$ , representing the power inside the slab over the total power including evanescent decaying power over the air, had been derived in [18] and [39]. Following notations from [39], the TE mode power ratio,  $C_{TE}$ , is derived differently in this letter as follows:

$$k_{TE,2} \tan(k_{TE,2}a) = (\mu_{r2}/\mu_{r3})k_{TE,3}, \quad (1)$$

$$k_{TE,2}^2 + k_{TE,3}^2 = (\mu_{r2}\epsilon_{r2} - \mu_{r3}\epsilon_{r3})k_0^2. \quad (2)$$

where  $k_{TE,2}$  and  $k_{TE,3}$  are defined as the TE mode cutoff wave numbers.

$$C_{TE} = \frac{A_{TE}}{A_{TE} + B_{TE}}, \quad (3)$$

$$A_{TE} = \mu_{r2}k_{TE,3}^3(2k_{TE,2}a + \sin(2k_{TE,2}a)), \quad (4)$$

$$B_{TE} = 2\mu_{r3}k_{TE,2}^3 \sin^2(k_{TE,2}a), \quad (5)$$

where  $A_{TE}$  and  $B_{TE}$  are simplified terms that are proportional to the power propagating within the dielectric slab and the power propagating in air, respectively.

Fig. 2(c) shows the power ratio curves for TE and TM modes with  $\epsilon_r = 2, 4, 10.2, 25$ . It is evident that the power ratio of the TE mode surpasses that of the TM mode when the dielectric slab thickness per guided wavelength ( $h\sqrt{\epsilon_r}/\lambda_0$ ) is smaller than one quarter wavelength. This discrepancy becomes more pronounced when the thickness per guided wavelength decreases below 0.1. For example, at the chosen substrate thickness of 0.292 mm in this paper, corresponding to  $h\sqrt{\epsilon_r}/\lambda_0 = 0.042$ ,  $C_{TE}$  and  $C_{TM}$  are 0.112 and 0.00128, respectively, with  $\epsilon_r = 10.2$ . Notably,  $C_{TE}$  consistently exceeds  $C_{TM}$  for  $2 \leq \epsilon_r$ , when the thickness per guided wavelength is less than 0.1. Therefore, PMC ground proves to be superior to PEC ground when low profile is required, with even greater superiority at higher values of  $\epsilon_r$ .

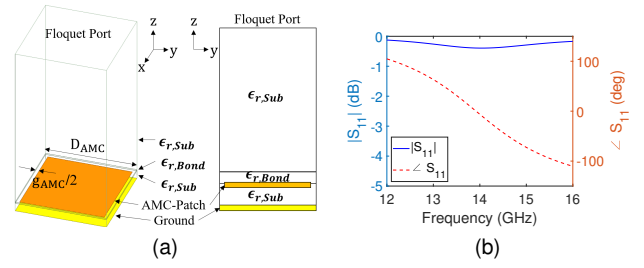


Fig. 3. (a) The designed AMC unit cell and (b) its reflection response. ( $D_{AMC}, g_{AMC}, \epsilon_{r,Sub}, \epsilon_{r,bond}$ ) = (2.75 mm, 0.2 mm, 10.2, 2.94).

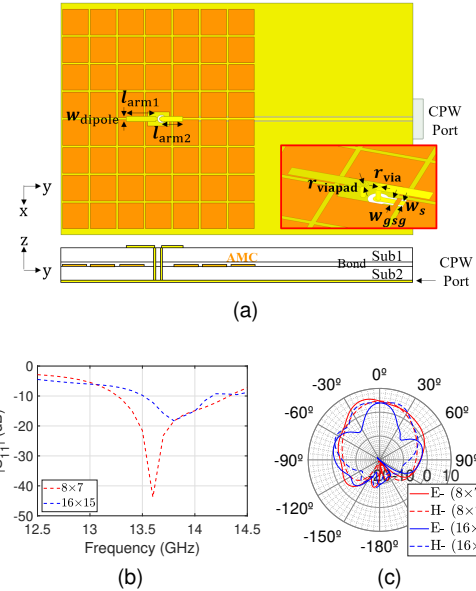


Fig. 4. (a) Configuration of the designed AMC-ground-integrated dipole antenna with  $8 \times 7$  AMC unit cells. The marked design parameters are ( $l_{arm1}, l_{arm2}, w_{dipole}, r_{via}, r_{viapad}, w_s, w_{gsg}$ ) = (2.9, 2.1, 0.5, 0.1, 0.2, 0.3, 0.5) mm. (b) Reflection coefficients and (c) co-polarized radiation patterns for  $8 \times 7$  and  $16 \times 15$  AMC unit cells at 14 GHz in the E- and H-planes.

## III. SURFACE WAVE LAUNCHER: HORIZONTAL DIPOLE ANTENNA WITH AMC GROUND

### A. AMC Ground for Low Profile SWL

The PMC ground is realized using the AMC ground [40]-[42], with the AMC unit cell shown in Fig. 3(a). Two 0.254 mm thick Rogers RT/duroid 6010/6010LM dielectric substrates ( $(\epsilon_{r,Sub}, \tan \delta) = (10.2, 0.0023)$ ) were attached using Rogers 2929 Bondply ( $(\epsilon_{r,Bond}, \tan \delta) = (2.94, 0.003)$ ) with a thickness of 0.038 mm. The medium between the Floquet port and the AMC surface in Fig. 3(a) is set to  $\epsilon_{r,sub}$  because the  $-z$ -directed radiation from the dipole feed propagates through the upper substrate (Sub1) and is reflected at the top surface of the AMC stack (Bond layer), as shown in Fig. 1; thus, the AMC surface is surrounded by Sub1 rather than air. Fig. 3(b) presents the simulated reflection phase of the AMC unit cell as a function of frequency. Using the  $\pm 90^\circ$  reflection-phase criterion, the practical AMC bandwidth is identified as 12.5–15.3 GHz.

Fig. 4 shows the designed SWL with the AMC ground. The HMA aperture size was determined to be  $44 \text{ mm} \times 41.25 \text{ mm}$

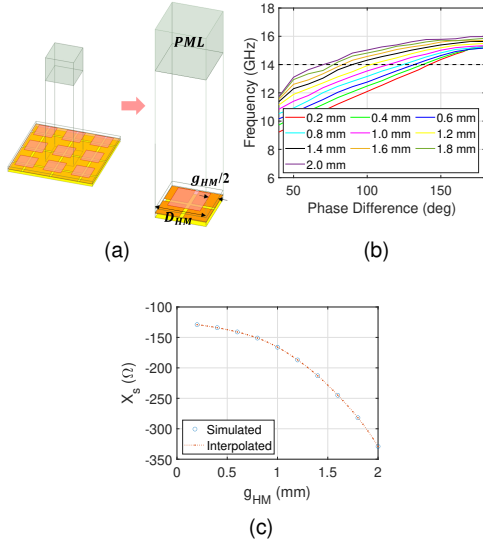


Fig. 5. (a) Configuration of the proposed HMUC and (b) its simulated dispersion curves with variation in  $g_{HM}$ . (c) The calculated TE mode surface reactance  $X_s = Im(Z_s)$  with variation in  $g_{HM}$ .

with  $16 \times 15$  AMC unit cells, which corresponds to  $4.86\lambda_g \times 4.56\lambda_g$ , where  $\lambda_g$  is defined as the guided wavelength.

#### IV. AMC-GROUND-INTEGRATED HMA DESIGN

##### A. HMUC Including AMC

Fig. 5(a) shows the HMUC with a size of  $2.75 \text{ mm} \times 2.75 \text{ mm}$ , identical to the AMC unit cell. The top patch is positioned at the vertex where four adjacent AMC unit cells meet, because the electric fields are naturally concentrated near the gap between the AMC patches. The TE mode surface impedance of an HMUC,  $Z_s$ , can be calculated as follows [43]:

$$Z_{TE} = \frac{E_x}{H_z} = j \frac{\omega \mu_3}{k_{TE,3}} = j \eta_0 \frac{k_0}{\sqrt{\beta^2 - k_0^2}} = \frac{\eta_0}{\sqrt{1 - n^2}}, \quad (6)$$

where the effective refractive index  $n$  is defined as follows:

$$n = \frac{\beta}{k_0} = \frac{\phi/D_{HM}}{\omega/c} = \frac{\phi c}{\omega D_{HM}}, \quad (7)$$

where  $\phi = \beta D_{HM}$  is the phase difference across a HMUC. Fig. 5(b) shows the dispersion curves drawn from HFSS Eigenmode solver. The TE mode surface wave reactance,  $X_s = Im(Z_s)$ , varying with  $g_{HM}$  is then derived, as shown in Fig. 5(c), where the maximum and minimum surface wave reactances are  $-129\Omega$  and  $-329\Omega$ . The capacitive surface impedance for TE mode has also been validated in [44].

##### B. HMA Design

In the radio-frequency domain, an HM realizes an interference pattern of impedance-modulated unit cells formed by the reference wave (RW),  $\psi_{ref}$ , and the object wave (OW),  $\psi_{obj}$  [11]. The SWL excites the surface wave ( $\psi_{ref}$ ); the HM then synthesizes the desired radiated wave ( $\psi_{obj}$ ). The required surface-impedance is calculated as follows:

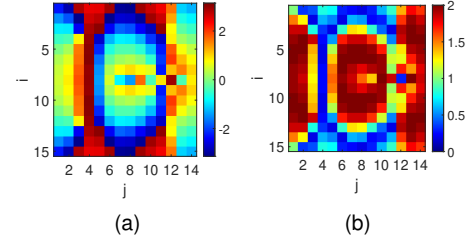


Fig. 6. (a)  $\phi_{ref}$  distribution and (b) calculated  $g_{HM}$  distribution with location indices  $i$  and  $j$ , and  $\phi_{offset} = \pi$  on the HMA aperture.

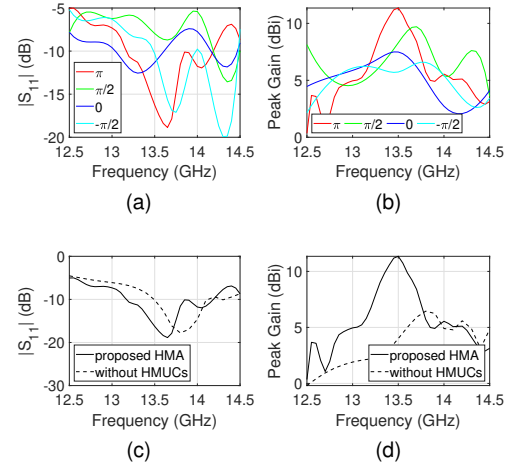


Fig. 7. (a) Simulated reflection coefficient and (b) peak gain for different values of  $\phi_{offset} = \pi, \pi/2, 0, -\pi/2$ . For the proposed ( $\phi_{offset} = \pi$ ) HMA, (c) simulated reflection coefficient and (d) peak gain with and without HMUCs.

$$Z_s = 1j \times [X + M \times Re(\psi_{ref}^* \psi_{obj})], \quad (8)$$

where  $X$  represents the average of the available maximum and minimum surface wave reactance,  $-229\Omega$  in this letter.

The reference surface-wave phase  $\phi_{ref}$  in Fig. 6(a) was extracted from full-wave HFSS by sampling the phase of the y-polarized electric field at the center of each unit cell on the metasurface plane, yielding a  $15 \times 14$  phase map. This full-wave extraction naturally includes edge reflections and CPW-feed coupling effects. Although  $\phi_{ref}$  is empirically extracted from full-wave simulation, the final performance is not highly sensitive to small phase perturbations because the holographic metasurface primarily enforces a global constructive-phase condition. Thus, moderate local deviations mainly affect secondary features, and no iterative optimization was needed after implementing the impedance map.

Assuming little traveling wave power loss,  $\psi_{ref} = \exp(j\phi_{ref})$ , and  $\psi_{obj} = \exp(j\phi_{obj})$ , (8) is rewritten:

$$Z_s = 1j \times [X + M \cos(-\phi_{ref} + \phi_{obj})]. \quad (9)$$

Notably, for a broadside beam pattern,  $\phi_{obj} = \phi_{offset}$ , where  $-\pi \leq \phi_{offset} \leq \pi$  is a constant. By combining (6) and (9), the calculated  $g_{HM}$  distribution with  $\phi_{offset} = \pi$  across the HMA aperture is shown in Fig. 6(b).

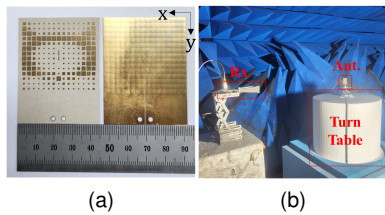


Fig. 8. Photographs of the (a) fabricated sample and (b) measurement setup in the anechoic chamber.

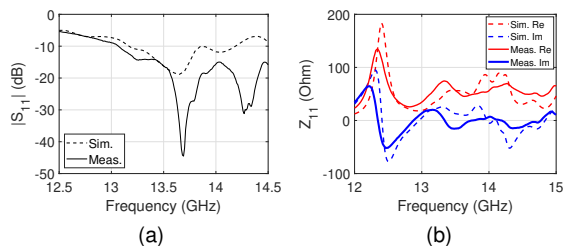


Fig. 9. The simulated and measured (a) reflection coefficient ( $|S_{11}|$ ) and (b) input impedance ( $Z_{11}$ ).

Fig. 7(a) and Fig. 7(b) show the reflection coefficient and peak gain with varying  $\phi_{offset}$ . The variation in impedance bandwidth and peak realized gain arise from electromagnetic coupling between the SWL and the nearest HMUCs. The proposed broadside-beam HMA is designed with  $\phi_{offset} = \pi$ , which yields the best  $|S_{11}|$  and peak realized gain because the SWL-surrounding HMUC patches are smallest. Fig. 7(c) and Fig. 7(d) compare the reflection coefficient and peak gain of the proposed HMA with and without HMUCs. Introducing HMUCs significantly enhances the peak gain while preserving the impedance bandwidth.

## V. FABRICATION AND MEASUREMENT

### A. Measurement Results

The proposed TE-mode unidirectional HMA is fabricated and measured. Fig. 8 shows the fabricated sample and the measurement setup in the anechoic chamber. The edge-launch connector is connected to the end of the CPW line.

Fig. 9 shows the simulated and measured reflection coefficient ( $|S_{11}|$ ) and input impedance ( $Z_{11}$ ). The measured impedance bandwidth is slightly wider than the simulated 1.02 GHz (13.17–14.19 GHz). The simulation–measurement discrepancy in Fig. 9(a) is mainly due to fabrication tolerances that perturb the input impedance, while the resonance frequencies remain close within 1.6% deviation. Since the antenna is near matched, small impedance shifts around  $50\Omega$  can cause a large change in the  $|S_{11}|$  notch depth.

Fig. 10(a) shows the simulated and measured radiation patterns in H- and E-planes, at 13.5 GHz and 13.6 GHz, respectively, where the simulated and measured peak gain of 11.35 dBi and 11.19 dBi are observed, respectively. The proposed antenna exhibits a high cross-polarization discrimination level of over 25 dB in the main beam direction, along with an excellent front-back-ratio of 25.2 dB. Fig. 10(b) shows

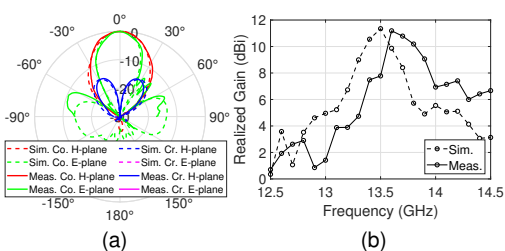


Fig. 10. (a) The simulated radiation patterns at 13.5 GHz and the measured radiation patterns at 13.6 GHz, both normalized by the peak gain, in the H-plane and E-plane. (b) The simulated and measured peak gain.

TABLE I  
COMPARISON OF STATE-OF-THE-ART PRACTICALLY DEMONSTRATED LOW-PROFILE UNIDIRECTIONAL HOLOGRAPHIC METASURFACE ANTENNAS

Ref.	Surface Wave Mode	Frequency (GHz)	Total Thickness, $t_{tot}$ ( $\lambda_0$ )	Aperture Efficiency (%)	FOM ( $\text{AE}/t_{tot}$ )	Ground Type
[24]	TM	11.5	0.096	29.7	<b>3.09</b>	PEC
[27]	TM	31.5	0.16	27.9	<b>1.74</b>	PEC
[37]	TE	61 <sup>*4</sup>	0.174 <sup>*5</sup>	20.4 (18.0)	<b>1.17</b> ( <b>1.03</b> )	No ground
<b>This work</b>	<b>TE</b>	<b>13.5</b>	<b>0.025</b>	<b>29.5</b> ( <b>27.7</b> )	<b>11.80</b> ( <b>11.08</b> )	<b>AMC</b>

<sup>\*1</sup> Assumed from the gain over frequency plot.

<sup>\*2</sup> AMC substrate thickness is assumed as that of the thinnest substrate.

the simulated and measured peak gain over frequency. The corresponding simulated and measured aperture efficiencies are 29.54% and 27.65%, respectively, at 13.5 GHz and 13.6 GHz. The simulated and measured radiation efficiencies are 51.5% and 49.7%, respectively, at 13.5 GHz and 13.6 GHz.

The proposed TE-mode HMA bandwidth and realized gain are limited by the AMC unit-cell bandwidth (12.5–15.3 GHz), as shown in Fig. 9(a) and Fig. 10(b). Accordingly, the dipole-with-AMC (13.3–14.3 GHz) and the HMA (13.1–14.2 GHz) operate within this range, and the gain degrades rapidly outside it as the AMC departs from PMC-like reflection.

### B. Discussion on Comparison With State-of-The-Arts

Table I compares practically demonstrated low-profile unidirectional HMAs. The FOM is defined as aperture efficiency divided by total thickness to capture the efficiency–profile trade-off. The proposed AMC-grounded HMA achieves comparable aperture efficiency with much smaller thickness than conventional PEC-grounded unidirectional HMAs, yielding a competitive FOM.

## VI. CONCLUSION

This letter presented an ultra-thin, unidirectional AMC-ground-integrated HMA based on TE-mode surface-wave excitation. We demonstrated, both theoretically and experimentally, that replacing a conventional PEC ground with a PMC/AMC ground increases the surface-wave power ratio for ultra-thin HMAs. The outlined design considerations for monolithic integration of the horizontal-dipole SWL, AMC ground, and holographic metasurface provide practical guidance for future research on AMC-ground-integrated HMAs.

## ACKNOWLEDGMENT

This work was supported by Samsung Electronics, MX division.

## REFERENCES

- [1] B. Xu *et al.*, "Investigation of surface waves suppression on 5G handset devices at 15 GHz," *Proc. 10th Eur. Conf. Antennas Propag.*, 2016, pp. 1–4.
- [2] O. Kagaya *et al.*, "Generation of surface wave in C-band automotive on-glass antenna and an easily realizable suppression method for improving antenna characteristics," *IEICE Trans. Comm.* Vol. 105, No. 1 pp. 51–57, Jan. 2022.
- [3] T. Yoon, U. Park and J. Oh, "Band-Stop Behavior Vertically Extended Ground Isolator Based on Transmission Line Theory for IBFD TRx Decoupling Applications," *IEEE Trans. Microw. Theory Techn.*, vol. 72, no. 2, pp. 1405–1415, Feb. 2024.
- [4] V. R. Komanduri *et al.*, "A General Method for Designing Reduced Surface Wave Microstrip Antennas," *IEEE Trans. Antennas Propag.*, vol. 61, no. 6, pp. 2887–2894, Jun. 2013.
- [5] K. Zhao *et al.*, "mmWave Phased Array in Mobile Terminal for 5G Mobile system with Consideration of Hand Effect," *IEEE 81st VTC Spring*, May 2015.
- [6] B. Kim *et al.*, "Heterogeneous Metasurface Empowering Proximate High-Permittivity Ceramic Cover for a 5G Dual-Band Millimeter-Wave Smartphone," *IEEE Trans. Antennas Propag.*, vol. 72, no. 5, pp. 4086–4094, May 2024.
- [7] B. Kim and J. Oh, "Dual-Wideband Low-Profile Three-Notch Patch Antenna With Indirect Differential Feeding for 5G Millimeter-Wave Applications," *IEEE Antennas Wireless Propag. Lett.*, vol. 24, no. 9, pp. 2734–2738, Sep. 2025.
- [8] R. Rodriguez-Cano, S. Zhang, and G. F. Pedersen, "Transparent mm-wave array on a glass substrate with surface wave reduction," *Proc. 14th Eur. Conf. Antennas Propag. (EuCAP)*, Jul. 2020, pp. 1–4.
- [9] B. Kim, S. Bang, S. Yun, H. Kim, and J. Oh, "Broadband Holographic Mode Synthesis Between Adjacent Resonances for a Low-Profile Thin-Microstrip Antenna-Fed Metasurface," *IEEE Trans. Antennas Propag.*, vol. 73, no. 11, pp. 9577–9582, Nov. 2025.
- [10] B. Kim, S. Hwangbo, and J. Oh, "Optically Transparent Holographic Display Antenna: High Gain, Beam Steering, and Lossless Bonding for 5G Millimeter-Wave n261 Band," *IEEE Open J. Antennas Propag.*, vol. 6, no. 6, pp. 1799–1814, Dec. 2025.
- [11] B. H. Fong *et al.*, "Scalar and Tensor Holographic Artificial Impedance Surfaces," *IEEE Trans. Antennas Propag.*, vol. 58, no. 10, pp. 3212–3221, Oct. 2010.
- [12] G. Minatti *et al.*, "Spiral Leaky-Wave Antennas Based on Modulated Surface Impedance," *IEEE Trans. Antennas Propag.*, vol. 59, no. 12, pp. 4436–4444, Dec. 2011.
- [13] S. Bang *et al.*, "Extremely Miniaturized Free-Space Measurement System for RF Metamaterial Composite Based on Beam Focusing Transmittarray," *IEEE Antennas Wireless Propag. Lett.*, vol. 23, no. 6, pp. 1705–1709, June 2024.
- [14] B. Kim and J. Oh, "Single-Glass-Layer Optically Transparent Transmittarray With High Aperture Efficiency and Low Profile at 5G Millimeter-Wave Band," *IEEE Trans. Antennas Propag.*, vol. 71, no. 11, pp. 9036–9041, Nov. 2023.
- [15] B. Kim *et al.*, "Locally Optimal Periods in Periodic Optically Transparent Two-Metal-Layered Refractive Metasurfaces for Outdoor-to-Indoor Communication," *IEEE Antennas Wireless Propag. Lett.*, vol. 24, no. 5, pp. 1253–1257, May 2025.
- [16] H. -H. Lv *et al.*, "Holographic Design of Beam-Switchable Leaky-Wave Antenna," *IEEE Antennas Wireless Propag. Lett.*, vol. 18, no. 12, pp. 2736–2740, Dec. 2019.
- [17] Z. L. Ma *et al.*, "A Collimated Surface-Wave-Excited High-Impedance Surface Leaky-Wave Antenna," *IEEE Antennas Wireless Propag. Lett.*, vol. 16, pp. 2082–2085, 2017.
- [18] Z. Chen and Z. Shen, "Wideband Flush-Mounted Surface Wave Antenna of Very Low Profile," *IEEE Trans. Antennas Propag.*, vol. 63, no. 6, pp. 2430–2438, June 2015.
- [19] Z. Hu, Z. Shen, and W. Wu, "Reconfigurable Leaky-Wave Antenna Based on Periodic Water Grating," *IEEE Antennas Wireless Propag. Lett.*, vol. 13, pp. 134–137, 2014.
- [20] T. Galler *et al.*, "High-Gain Millimeter-Wave Holographic Antenna in Package Using Glass Technology," *IEEE Antennas Wireless Propag. Lett.*, vol. 19, no. 12, pp. 2067–2071, Dec. 2020.
- [21] L. Gan *et al.*, "Low Profile Circularly Polarized Holographic Antenna with Improved Aperture Efficiency," *Proc. Int. Conf. Microw. Millimeter Wave Technol. (ICMMT)*, 2023, pp. 1–3.
- [22] Y. Liu *et al.*, "Low RCS and High-Gain Patch Antenna Based on a Holographic Metasurface," *IEEE Antennas Wireless Propag. Lett.*, vol. 18, no. 3, pp. 492–496, March 2019.
- [23] S. K. Podilchak, A. P. Freundorfer and Y. M. M. Antar, "Broadside Radiation From a Planar 2-D Leaky-Wave Antenna by Practical Surface-Wave Launching," *IEEE Antennas Wireless Propag. Lett.*, vol. 7, pp. 517–520, 2008.
- [24] J. -L. Liu, T. Su and Z. -X. Liu, "High-Gain Grating Antenna With Surface Wave Launcher Array," *IEEE Antennas Wireless Propag. Lett.*, vol. 17, no. 4, pp. 706–709, April 2018.
- [25] J. Cavillot, M. Bodehou, and C. Craeye, "Metasurface antennas design: Full-wave feeder modeling and far-field optimization," *IEEE Trans. Antennas Propag.*, vol. 71, no. 1, pp. 39–49, Jan. 2023.
- [26] M. Faenzi *et al.*, "Metasurface antennas: New models, applications and realizations," *Sci. Rep.*, vol. 9, no. 1, p. 10178, Jul. 2019.
- [27] D. González-Ovejero *et al.*, "Additive Manufactured Metal-Only Modulated Metasurface Antennas," *IEEE Trans. Antennas Propag.*, vol. 66, no. 11, pp. 6106–6114, Nov. 2018.
- [28] G. Minatti, E. Martini, and S. Maci, "Efficiency of metasurface antennas," *IEEE Trans. Antennas Propag.*, vol. 65, no. 4, pp. 1532–1541, Apr. 2017.
- [29] M. Bodehou *et al.*, "Power balance and efficiency of metasurface antennas," *Sci. Rep.*, vol. 10, no. 1, p. 17508, Oct. 2020.
- [30] S. Xue, *et al.*, "Double-Layer Cross-Embedded Holographic Antennas with Compact Size and High Efficiency," *IEEE Trans. Antennas Propag.*, vol. 72, no. 7, pp. 5436–5446, Jul. 2024.
- [31] D. M. Pozar, "Surface wave effects for millimeter wave printed antennas," *Proc. Antennas Propag. Soc. Int. Symp.*, 1983, vol. 21, pp. 692–695.
- [32] M. Movahhedi, M. Karimipour and N. Komjani, "Multibeam Bidirectional Wideband/Wide-Scanning-Angle Holographic Leaky-Wave Antenna," *IEEE Antennas Wireless Propag. Lett.*, vol. 18, no. 7, pp. 1507–1511, July 2019.
- [33] F. Ge *et al.*, "Bidirectional Scanning Antenna Based on Surface Wave Mode," *IEEE Antennas Wireless Propag. Lett.*, vol. 21, no. 8, pp. 1592–1596, Aug. 2022.
- [34] A. Moshiri and A. Amini, "Non-linear least squares optimization for the design of low side lobe level bidirectional holographic antennas," *AEU—Int. J. Electron. Commun.*, pp.154944, 2023.
- [35] A. Araghi *et al.*, "Holographic-Based mmW-Wideband Bidirectional Frequency Scanning Leaky Wave Antenna," *14th Eur. Conf. Antennas Propag. (EuCAP)*, 2020, pp. 1–5.
- [36] M. Li, S. -Q. Xiao and D. F. Sievenpiper, "Polarization-Insensitive Holographic Surfaces With Broadside Radiation," *IEEE Trans. Antennas Propag.*, vol. 64, no. 12, pp. 5272–5280, Dec. 2016.
- [37] C. Rusch *et al.*, "Holographic mmW-Antennas With TE0 and TM0 Surface Wave Launchers for Frequency-Scanning FMCW-Radars," *IEEE Trans. Antennas Propag.*, vol. 63, no. 4, pp. 1603–1613, April 2015.
- [38] M. Li, Y. Zhang and M. -C. Tang, "A Horizontally-Polarized, Broadside, Holographic Antenna Design with Rotationally-Symmetric Beam," *11th UK-Eur.-China Workshop Millimeter Waves Tera. Technol. (UCMMT)*, 2018, pp. 1–3.
- [39] S. S. Attwood, "Surface-wave propagation over a coated plane conductor," *J. Appl. Phys.*, vol. 22, no. 4, pp. 504–509, Apr. 1951.
- [40] A. P. Feresidis *et al.*, "Artificial magnetic conductor surfaces and their application to low-profile high-gain planar antennas," *IEEE Trans. Antennas Propag.*, vol. 53, no. 1, pp. 209–215, Jan. 2005.
- [41] R. Dewan *et al.*, "Artificial magnetic conductor for various antenna applications: An overview," *Int. J. RF Microw. Comput.-Aided Eng.*, vol. 27, no. 6, Aug. 2017, Art. no. e21105.
- [42] J. Zhu, S. Li, S. Liao and Q. Xue, "Wideband Low-Profile Highly Isolated MIMO Antenna With Artificial Magnetic Conductor," *IEEE Antennas Wireless Propag. Lett.*, vol. 17, no. 3, pp. 458–462, Mar. 2018.
- [43] D. M. Pozar, *Microwave Engineering*, 3rd ed. Hoboken, NJ, USA: Wiley, 2005.
- [44] M. Li, S. Xiao, J. Long, and D. Sievenpiper, "Surface Waveguides Supporting Both TM Mode and TE Mode with the Same Phase Velocity," *IEEE Trans. Antennas Propag.*, vol. 64, no. 9, pp. 3811–3819, Sep. 2016.